Tropospheric water vapor imaging by combination of ground-based and spaceborne GNSS sounding data

Ulrich Foelsche and Gottfried Kirchengast

Institute for Geophysics, Astrophysics, and Meteorology (IGAM), University of Graz, Graz, Austria

Abstract. The Global Navigation Satellite System (GNSS) comprises the U.S. system GPS (Global Positioning System), its Russian pendant GLONASS, and presumably, in the future, the European system Galileo. The potential of GNSS-based phase delay measurements for accurately estimating vertically and slant-path-integrated water vapor has been demonstrated recently for radio links between GPS satellites and ground-based GPS receivers. GNSS-based radio occultation, on the other hand, has been demonstrated via the GPS/Meteorology experiment to deliver accurate near-vertical profiles of atmospheric variables such as temperature and humidity with high vertical resolution. Height-resolving imaging of atmospheric water vapor becomes feasible when occultation profiles from spaceborne receivers in Low Earth Orbits (LEO) are combined with ground-based GNSS data from a colocated receiver network. We developed a two-dimensional, height-resolving tomographic imaging technique following the Bayesian approach for optimal combination of information from different sources. Using simulated GNSS-based water vapor measurements from LEO and ground, we show representative results derived from simple synthetic refractivity fields as well as from a realistic refractivity field based on a European Centre for Medium-Range Weather Forecasts (ECMWF) analysis. For cases located poleward of ~ 40° we found a new simple mapping function to perform best within our forward model scheme, where the only free parameter is the climatological scale height in the troposphere, the exact value of which is not critical. The mapping function exploits the ratio between the straight-line ray path length within the first two scale heights above surface and the "effective height" defined by these first two scale heights. We found our technique capable of reconstructing atmospheric features like water vapor maxima near the top of the trade wind inversion. Adjustment of the integral over the water vapor profile measurements to the horizontally averaged ground-based vertical integrated water vapor data efficiently mitigates potential biases in the former data. Accuracies are best in areas with high absolute humidities but also over drier areas such as Finland, useful two-dimensional information can still be obtained. Thus it is attractive to apply the developed technique in a next step to real data.

1. Introduction

A deeper understanding of the mechanisms distributing water vapor through the atmosphere and of water the vapor effects on atmospheric radiation and circulation is vital to estimate long-term changes in climate. This understanding is hampered by the fact that water vapor is the most variable of the major constituents of the atmosphere, and our ability to measure time-varying global and regional water vapor distributions is still severely limited.

Emerging networks of continuously operating GPS receivers provide a new and powerful approach to remote sensing of atmospheric water vapor [*Bevis et al.*, 1992]. The GPS consists of a constellation of 24 satellites that transmit L-band radio signals to large numbers of users primarily engaged in navigation and geodesy. These signals are delayed by the atmospheric water vapor while they propagate from GPS satellites to ground-based receivers.

This "geodetic noise" is a valuable meteorological signal, as the so-called wet delay is nearly proportional to the quantity of water vapor integrated along the signal path, which in turn can be transformed into an estimate of precipitable water. Given accurate delay measurements, precipitable water can be recovered with an accuracy of ~ 1 mm [*Elgered et al.*, 1997].

A slightly different approach allows sensing of integrated slant-path water vapor along ray paths between GPS satellites and receivers [*Ware et al.*, 1997]. In principle, it is possible to use signals from the Russian global navigation satellite system (GLONASS) in exactly the same way as described above, though the number of GLONASS receivers in use is still small compared to the number of GPS receivers. Furthermore, the planed European GALILEO system will be another valuable future signal source. We thus, generally, use the term GNSS (global navigation satellite system), comprising all these systems.

Another GNSS-based remote sensing application is the radio occultation technique, which uses a satellite-to-satellite limb-sounding concept to probe the Earth's atmosphere [e.g., *Kursinski et al.*, 1997]. From the point of view of a GNSS receiver aboard a Low Earth Orbit (LEO) satellite an

occultation occurs whenever a GNSS satellite rises or sets near the Earth's limb, and the ray path from the transmitter traverses the Earth's atmosphere toward the receiver.

The influence of the atmospheric refractivity field on the propagation of the electromagnetic signal enables the retrieval of atmospheric refractivity profiles and the derivation of further parameters such as density, pressure, and temperature. In the lower and midtroposphere, refractivity variations are dominated by water vapor (especially at low latitudes), and high vertical resolution humidity profiles can be retrieved, given independent temperature data.

The combination of these two complementary information sources allows the retrieval of two-dimensional, height-resolving water vapor density fields employing tomographic reconstruction techniques. The emphasis of this work was to develop a sensible technique for this type of water vapor imaging. Such a data product could contribute to the provision of much needed information on regional and global water vapor distributions.

In section 2 the employed forward modeling is described, which is an important part of the study as we worked, at this developmental stage, with simulated rather than real data. Sections 3 and 4 then introduce the optimal estimation approach and the reconstruction geometry used, respectively. Imaging results are subsequently described in sections 5 (for cases using simple synthetic water vapor data) and 6 (for cases using data derived from a European Centre for Medium-Range Weather Forecasts (ECMWF) analysis field). Section 7 provides a summary and the main conclusions of the study.

2. Forward Modeling

2.1. Geometry

To demonstrate the feasibility of water vapor imaging, we selected a somewhat idealized but not unrealistic geometry. We considered a two-dimensional planar cut through the neutral atmosphere, hereinafter termed reconstruction plane, which can be thought of to be defined by the sounding plane of an occultation event.

The domain of the reconstruction plane, as used for the forward modeling (FOMOD), is divided into 45,000 picture elements (pixels). The height interval between 0 km and 10 km is represented by 100 layers with 100 m vertical width, the interval between 10 km and 50 km by 200 layers with 200 m vertical width. In the horizontal domain we divided the plane into 150 equidistant latitudinal sectors with a width of 0.05° (corresponding to 5.6 km width at the surface), the sector thus spans a total width of 7.5° (~ 800 km). The corresponding reconstruction setup, utilizing only a subdomain of this FOMOD domain, is described in section 4.

In general, the ground receiver and satellite positions will laterally deviate somewhat from the reconstruction plane and thus introduce corresponding deviations of sounding links. This problem can be overcome by introducing "three-dimensional pixels" with a certain extent perpendicular to the occultation plane [Leitinger et al., 1997], or by performing, in preprocessing, a projection of rays into this plane.

For our simulations we assumed a vertical occultation event, aligned with (and centered with respect to) a meridionally oriented chain of 10 equidistant ground-based receivers. A considerable number of occultation events can be approximated by a vertical plane [Foelsche and Kirchengast, 1997]. The ground stations are assumed to be separated by 0.25° (27.8 km), comparable to spacings in existing dense networks. In practice, one would use a subset of stations of a given receiver network, which is best colocated with the occultation plane.

For a ground-based receiver, 5 to 12 GPS satellites above 5° elevation are in view at a given time [Hofmann-Wellenhof et al., 1994]. If signals from GLONASS satellites can be used in addition, the number nominally doubles.

We assumed three GNSS satellites to be approximately coplanar with the occultation plane. One satellite is located near the zenith, the two others near the horizon. These assumptions are not unrealistic even for the pure GPS case [see Ware et al., 1997, Figure 3]. The time interval was restricted to 30 min, a period during which the atmospheric water vapor field can be reasonably assumed as constant under typical atmospheric conditions. Within a 30 min period a GNSS satellite moves approximately 15° across the sky.

Assuming a signal integration time of about 4 min per transmitter-to-receiver ray [cf. Rocken et al., 1993], we considered eight rays per satellite, leading to a total number of 240 rays for ten stations each receiving three satellites.

We selected an elevation cutoff angle of 7°, comparable to cutoff angles used in field experiments in order to minimize multipath effects. The "geometric delay" due to ray bending is about 3 cm at an elevation angle of 10° and 10 cm at 5°, where the atmospheric phase delay reaches ~ 24 m [e.g., Elgered, 1993]. At elevations above 7°, ray bending can therefore be neglected, and the rays can be considered as straight lines, simplifying the forward model considerably.

When performing the forward modeling, i.e., the generation of quasi-realistic measurement data, we employed two different approaches, a simple one and a more realistic one, as described in sections 2.2 and 2.3, respectively, below.

2.2. Synthetic Refractivity Fields

To basically understand and check the performance of the reconstruction algorithm, we investigated several scenarios based on simple synthetic water vapor density fields which we constructed analytically. The synthetic model fields are displayed and described in sections 5.1 and 5.2, respectively, and discussed in comparison with the reconstructed fields.

In these analytical water vapor density scenarios we focused on learning about characteristic features of the retrieval algorithm and not on a quasi-realistic representation of the measurement procedure. Forward modeling in these cases thus just meant that slant-integrated water vapor (SIWV) along the different ray paths through the analytical density fields was computed and randomly perturbed by typical errors described in section 5 together with the corresponding covariance matrices. These synthetic SIWV data were then used as direct input for the reconstruction algorithm.

2.3. ECMWF-Derived Refractivity Fields and Excess Path Delays

To have a realistic forward computation of SIWV, we followed exactly the full procedure from excess phase paths to SIWV as described, for example, by Bevis et al. [1994] and Ware et al. [1997]. These FOMOD simulations, and the subsequent inversion to water vapor images, aimed at

demonstrating the feasibility of tomographic water vapor imaging in a realistic manner.

ECMWF analysis data of October 20, 1995 (an arbitrarily selected day), were used to construct realistic refractivity fields. The ECMWF data, available as gridded data at 1° x 1° horizontal sampling (original resolution = T213) at 31 model levels, were interpolated using cubic splines in order to fit the FOMOD pixel geometry (section 2.1). For temperature and specific humidity, values at the center of the pixels were taken as representative for the pixel area.

For total atmospheric pressure we assumed, in order to minimize the discretization error, exponential decrease with height within each pixel, with a local scale height corresponding to the temperature at the center of the pixel and computed the resulting mean pressure within the pixel, invoking the pressure at the lower edge of the pixel (the surface pressure in case of the lowest pixel).

The ECMWF profiles extend only to a height of about 30 km. Neglecting the influence of the atmosphere above 30 km introduces an unacceptable error into the forward model. To overcome this problem, we used MSISE-90 climatological data [Hedin, 1991] for the height interval between 30 km and 50 km, performing a smoothing transition between the two different profiles.

The refractivity N was computed using the Thayer [1974] equation with the constants proposed by Bevis et al. [1994]:

$$N \equiv (n-1)10^6 = k_1 \frac{p_d}{T} Z_d^{-1} + k_2 \frac{e}{T} Z_w^{-1} + k_3 \frac{e}{T^2} Z_w^{-1}; \qquad (1)$$

$k_1 = 77.60 \pm 0.05$ K/hPa,
$k_2 = 70.4 \pm 2.2$ K/hPa,
$k_3 = (3.739 \pm 0.012)\ 10^5$ K^2/hPa,

where n is the refractive index, p_d is the partial pressure of "dry air" in hectopascal, e is the partial pressure of water vapor in hPa, and T is the absolute temperature in K. Z_d^{-1} and Z_w^{-1} are the inverse compressibility factors for dry air and water vapor, respectively; these close-to-unity factors describe the nonideal gas behavior and have been expressed as given by Thayer [1974].

We considered the influence of the neutral atmosphere only, making the reasonable assumption that the ionospheric delay can be virtually removed (to 1 mm accuracy) using appropriate correction techniques [e.g., Brunner and Gu, 1991]. As we assume straight line propagation and constant refractivity within the picture elements, the excess path for each particular ray can be written in the form of the approximated optical path integral

$$\Delta L = \int_S (n-1)ds \cong 10^{-6} \sum_i N_i s_i , \qquad (2)$$

where s_i is the ray path length in pixel i, and N_i is the corresponding refractivity. The excess path data were randomly perturbed by a realistic root-mean-square (RMS) error of 2 mm, capturing receiver noise and unmodeled ionospheric effects.

2.4. From Excess Path Delay and Surface Pressure to Slant Wet Delay

Taking the surface pressure values of the ECMWF data sets, zenith hydrostatic delays ΔL^0_h at the ten ground stations

can be computed following Davis et al. [1985] and Elgered [1993]:

$$\Delta L^0_h = \frac{k_1 R^*}{10^6 m_d\ g_m} \frac{p_0}{f(\varphi, H)}, \qquad (3)$$

where p_0 is the total atmospheric pressure at the height of the antenna in hPa, R^* is the universal gas constant (8.314510 ± 0.000070 J K^{-1} mol^{-1}), m_d is the molar mass of dry air (28.9644 ± 0.0014) kg/kmol [Lide, 1993], and g_m = 9.7837 m/s^2. The variations of g_m with geographic latitude φ (in degrees) and the height above the geoid H (in kilometers) can be described as [cf. Davis et al., 1985]

$$f(\varphi, H) = 1 - 0.00265 \cos 2\varphi - 0.000285H . \qquad (4)$$

Combining the constants and their uncertainties (assumed uncorrelated) leads to:

$$\Delta L^0_h = [(0.0022768 \pm 0.0000015)\ \text{m hPa}^{-1}] \frac{p_0}{f(\varphi, H)}. \qquad (5)$$

Note that Davis et al. [1985] come to a slightly different error estimation, as they assume a smaller uncertainty in k_1.

For the surface pressure measurements we assumed and applied a realistic RMS error of 0.2 hPa. Slant hydrostatic delays along the ray paths to the different GPS satellites with elevation ε were obtained using the mapping function, $m(\varepsilon)$, given by Niell [1996] (hereinafter referred to as the Niell mapping function) or a newly developed "geometric" mapping function briefly introduced in section 2.5. The slant wet delay ΔL_w is then the difference of the measured excess path delay ΔL and the zenith hydrostatic delay mapped into the direction of the GPS satellite, $\Delta L_h = \Delta L^0_h\ m(\varepsilon)$,

$$\Delta L_w = \Delta L - \Delta L_h = \Delta L - \Delta L^0_h\ m(\varepsilon). \qquad (6)$$

An example, located in Florida, illustrating these three different delays is shown in Figure 1.
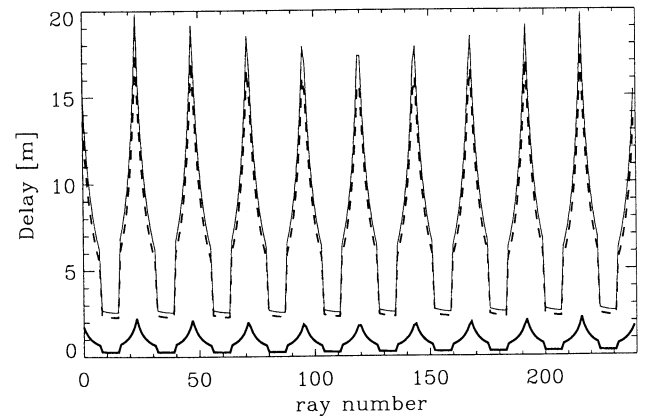

Figure 1. Excess path delay (light solid line), slant hydrostatic delay (dashed), and slant wet delay (thick solid line) for a refractivity field located in Florida (centered near Palm Beach, 27°N, 80°W), using the experimental setup described in the text. The leftmost 24 ray numbers correspond to ray paths between the different satellite positions and the first ground station, the second 24 ray numbers to the second ground station, etc.

2.5. The "Geometric" Mapping Function

We have developed a simple mapping function $m(\varepsilon)$ where the only free parameter is the climatological scale height. The value of $m(\varepsilon)$ is given by the ratio of the slant straight-line ray path length S_{atm} within an "effective height" of the atmosphere, H_{atm}, defined by the first two scale heights above the surface, and H_{atm} itself

$$m(\varepsilon) = \frac{S_{atm}}{H_{atm}} . \qquad (7)$$

Equation (7), alternatively, can be written as

$$m(\varepsilon) = \frac{1}{\sin\varepsilon \dfrac{S_{flat}}{S_{atm}}}, \qquad (8)$$

which directly illustrates the deviation from the simple cosecant law. S_{flat} is the corresponding ray path length in a "flat" atmosphere, in which the "geometric" mapping function degenerates to the cosecant law since $S_{atm} = S_{flat}$ in this case. S_{atm} can be determined for the realistic spherical atmosphere by evaluation of the triangle formed by R_e, $R_e + H_{atm}$, and S_{atm}, where R_e is the radius of the Earth (or the local radius of curvature, depending on the desired accuracy). In general, it is sufficient to use a mean climatological scale height value of 7.5 km, yielding $H_{atm} = 15.0$ km, as a globally applied constant. Introducing, for convenience, the ratio

$$\tilde{r} = \frac{R_e}{R_e + H_{atm}}, \qquad (9)$$

the path length within the effective height H_{atm} can be expressed as

$$S_{atm} = (R_e + H_{atm})[\cos(\arcsin(\tilde{r}\cos\varepsilon)) - \tilde{r}\sin\varepsilon], \qquad (10)$$

and equation (7), the "geometric" mapping function, then explicitly reads

$$m(\varepsilon) = \left(\frac{R_e}{H_{atm}} + 1\right)[\cos(\arcsin(\tilde{r}\cos\varepsilon)) - \tilde{r}\sin\varepsilon]. \qquad (11)$$

Comparing derived and "true" slant water vapor contents, we obtained the best results using the Niell mapping function at low latitudes (up to 40°), and the "geometric" mapping function poleward of 40°. The new mapping function is discussed in more detail in a forthcoming paper [*Foelsche and Kirchengast*, subm. manuscript, 2001], where its performance is quantitatively compared to other established mapping functions.

2.6. From Slant Wet Delay to Slant Integrated Water Vapor

The slant integrated water vapor (SIWV, measured in kg/m²) is nearly proportional to the slant wet delay ΔL_w :

$$SIWV \equiv \int_S \rho_w ds \cong \Pi \, \Delta L_w . \qquad (12)$$

The factor Π (units kg/m³) can be expressed after *Bevis et al.* [1992] as

$$\Pi = \frac{10^6 \, m_w}{\left(k_2 - k_1 \dfrac{m_w}{m_d} + \dfrac{k_3}{T_m}\right)R^*}, \qquad (13)$$

where m_w is the molar mass of water vapor (18.01528 kg/kmol) [*Lide*, 1993], and T_m is a "mean weighted" temperature of the atmosphere which can be modeled as $T_m = 70.2 + 0.72 T_0$ with T_0 being the surface temperature [*Bevis et al.*, 1992].

We used the surface temperature values from the ECMWF data sets with no add-on measurement errors assumed, as these are negligible compared with the representativeness errors in T_m due to modeling them as a linear function of T_0. *Bevis et al.* [1992] report a RMS representativeness error of 4.74 K or ~2%. Employing station-specific linear regression, this error can be reduced to ~1% [*Ross and Rosenfeld*, 1997].

The resulting RMS SIWV errors in the realistic scenario are on the order of ~2 kg/m². Figure 2 summarizes, in a schematic form, the method used to obtain simulated SIWV measurements.

3. Image Reconstruction by Optimal Estimation

Within the framework of discrete inverse theory, which we adopt for this work, the present forward modeling and reconstruction problems can be considered as algebraic mappings between vector spaces [*Rodgers*, 1976]. In the forward model, a linear operator **A** (typically called forward operator, observation operator, or the design matrix), which represents the act of measuring, describes the mapping from the state space into the measurement space (apart from the measurement error ε). **A** is a $m \times n$ matrix corresponding to m equations (measurements) and n unknowns (elements of the state vector). The forward model corresponds to a system of linear equations, which can be written as

$$\mathbf{y} = \mathbf{A}\,\mathbf{x} + \varepsilon , \qquad (14)$$

where the measurement vector **y** contains the (simulated) SIWV measurements along the different ray paths, **A** is the matrix of ray path lengths within the retrieval pixels, the state vector **x** contains the water vapor densities within the picture elements, and ε is the measurement error vector. The design matrix **A** depends only on the geometry of the experiment as long as ray bending can be neglected (ray bending depends on the state **x** and renders the forward model nonlinear).

To solve the reconstruction problem, we have to find an operator for the inverse mapping from the measurement space into the state space. A straightforward solution would use the generalized inverse of **A**, $\mathbf{A}^{-g}$, where $\mathbf{A}^{-g} = (\mathbf{A}^T \mathbf{A})^{-1} \mathbf{A}^T$ with superscripts "T" and "-1" denoting transpose and inverse, respectively.

The inverse problem can then be written (with the reconstructed state vector $\mathbf{x}_{reco}$) as

$$\mathbf{x_{reco}} = \mathbf{A}^{-g}\,\mathbf{y} . \qquad (15)$$

For the present geometry of ground-to-GNSS rays, however, the reconstruction problem, though overdetermined, is very close to ill-conditioned (the condition number is ~ 10^{11}).

Given this ill-conditioning, it is generally unavoidable to incorporate additional or a priori information. Occultation
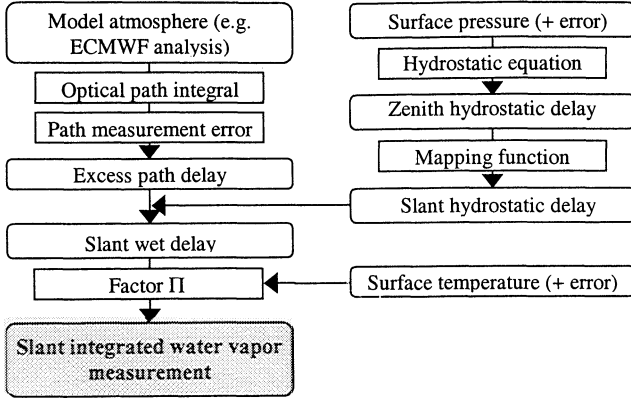
Figure 2. Forward model scheme for the realistic ECMWF scenario.

profiles are a very good candidate for such an a priori field. Because of the inherent along-ray integration they deliver a representative mean profile over a domain of the size of our reconstruction domain (the horizontal resolution of occultation profiles is ~270 km in the stratosphere and ~160 km near the surface [*Kursinski et al.*, 1997]).

The Bayesian approach provides a consistent theoretical framework to incorporate a priori information on the state, x_{ap}, in a transparent and explicit manner. We adopt this approach and a corresponding methodology, known as optimal estimation, a detailed description of which can be found in the work of *Rodgers* [2000]. In our case of a linear forward model and with the assumption of Gaussian probability distribution functions for the measurement and a priori errors, the reconstructed state vector is given by

$$x_{reco} = x_{ap} + (A^T S_\varepsilon^{-1} A + S_{ap}^{-1})^{-1} A^T S_\varepsilon^{-1} (y - Ax_{ap}), \quad (16)$$

where S_ε is the measurement error covariance matrix, and S_{ap} is the a priori error covariance matrix. The covariance matrix of the reconstructed state vector S_{reco} is given by

$$S_{reco} = (A^T S_\varepsilon^{-1} A + S_{ap}^{-1})^{-1}. \quad (17)$$

4. Reconstruction Geometry

With the exception of the domain size and the number of the picture elements, the reconstruction geometry is formally the same as the FOMOD geometry described in section 2.1. The domain of the reconstruction plane as used for the imaging on the basis of the simple synthetic SIWV data was divided into 200 picture elements (20 × 10). The height interval between 0 km and 10 km was represented by 20 layers with a respective height of 500 m. In the horizontal domain the plane was divided into 10 equidistant latitudinal sectors with a width of 0.25° (corresponding to 27.8 km at the surface), symmetric with respect to the ground stations.

In the case of realistic ECMWF-derived data the height of the imaging domain within the reconstruction plane was decreased to 6 km with 12 height layers (500 m each). The pixel number was therefore decreased to 120 (12 × 10).

Figure 3 illustrates the tomographic imaging setup for the case of the ECMWF data imaging. Note that the chosen aspect ratio (~1:22) is very much stretching the vertical against the horizontal scale; the most slant rays indicated are at 7° elevation angle (despite, they still look almost vertical with this aspect ratio).

5. Formulation of Error Covariance Matrices

5.1. A Priori Error Covariance Matrix

The a priori error covariance matrix S_{ap} was constructed on the basis of typical errors to be expected for a water vapor
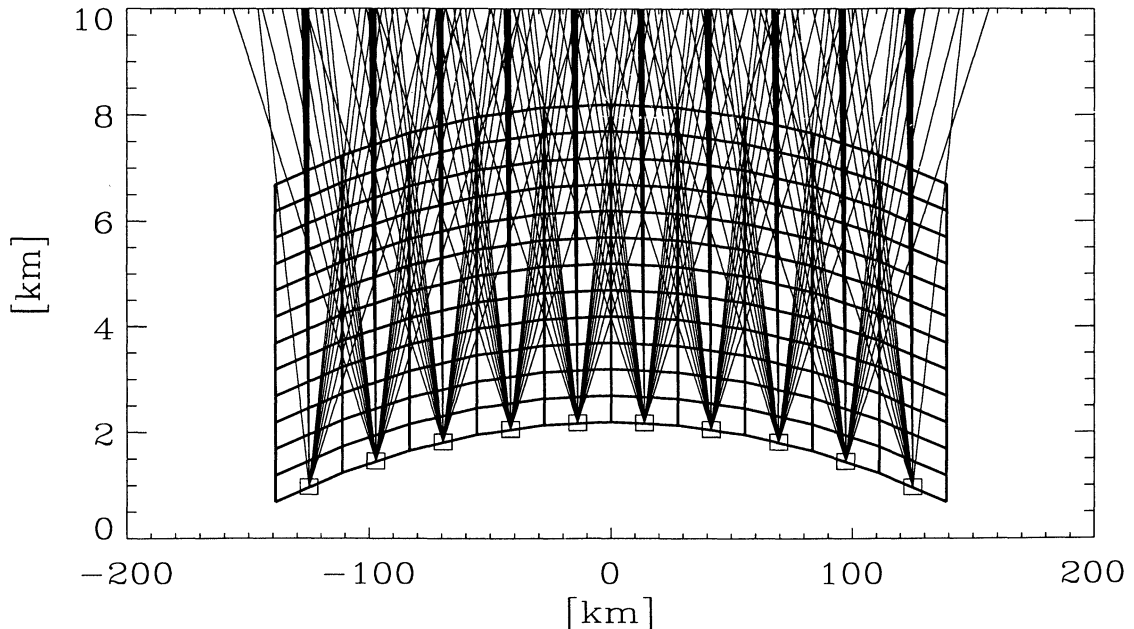

Figure 3. Reconstruction geometry (12 × 10 pixels) and rays from three satellites at 24 positions to ten ground stations (indicated by squares). A total of 226 rays is shown, as only rays not leaving the imaging domain sideward were used for the reconstruction process.

profile as derived from occultation data (by variational retrieval) [*Healy and Eyre*, 2000; *Kursinski et al.*, 1997]. At the surface the a priori water vapor density was assumed to be uncertain to 10% at domain center (the location of the occultation profile), linearly increasing to 25% uncertainty at the edges of the reconstruction domain, reflecting the decreasing representativeness of the occultation profile over its horizontal resolution scale. At the 10 km level the respective values were assumed to be 40% (center) and 100% (edge). The increase of uncertainty with height was assumed to be linear between the surface and 10 km. Regarding error correlation structure, we assumed a vertical error correlation length, L_v, of 3 km with exponential correlation decay structure, and a horizontal error correlation length L_h of 0.75° (~80 km) with Gaussian correlation decay structure, respectively. The elements of the a priori error covariance matrix are thus given by

$$S_{\text{ap } ik,jl} = \sigma_{ik}\sigma_{jl} \cdot \exp\left[-\frac{(x_j - x_i)^2}{L_h^2}\right] \exp\left[-\frac{|z_l - z_k|}{L_v}\right], \quad (18)$$

where x and z denote the horizontal and vertical coordinates, the subscript pairs ik and jl denote individual pixels between which the covariance is measured, and σ_{ik} and σ_{jl} denote the standard deviations associated with the individual pixels, which are obtained by multiplying the assumed relative errors with the corresponding pixel values of the a priori water vapor density field x_{ap}. The correlation lengths and correlation structures reasonably reflect both the vertical interdependence of errors in occultation-derived profiles due to nonlocal transforms involved (Abelian and hydrostatic integrations) [e.g., *Healy and Eyre*, 2000; *Rieder and Kirchengast*, 2001a,b] as well as the significant horizontal correlation over the horizontal resolution scale along the limb sounding rays.

The results presented below are found largely insensitive to the precise correlation lengths adopted (even zero correlation in both x and z does not change the results much). They are also weakly sensitive only to the exact magnitude of the covariance values in S_{ap}.

5.2. Measurement Error Covariance Matrix

In case of the measurement error we considered three different error contributions: uncorrelated observational error, correlated observational error, and discretization error.

The uncorrelated observational error, rooting in the excess path delay RMS error assumed to be ~2 mm vertically (section 2.3) [*Ware et al.*, 1997], can be expected to have an elevation angle dependence. Consistent with a vertical path delay error of 2 mm, we assumed a random SIWV error with an RMS of 0.4 kg/m$^2 \cdot m(\varepsilon)$, yielding 3.1 kg/m^2 at 7° elevation. Errors in the estimated mean temperature T_m [*Bevis et al.*, 1992], amounting to ~1% in the factor Π (equation (13)), tend to be highly correlated between the ground stations and they are mapped onto the ray path. Consistent with a 1% error in Π, we assumed an error of $0.01 \cdot \Pi \cdot \Delta L_w$ or $0.01 \cdot$ SIWV, resulting in typical SIWV errors of 0.3 kg/m^2 vertically and of 2.3 kg/m^2 at the 7° cutoff elevation angle.

The discretization error was determined by a few comparisons of SIWV integrations over a "true" field from either using the (fine) FOMOD or the (coarse) reconstruction grid. In each scenario, largely independent of the actual "true"

field selected, we found a negative bias of ~4% for all stations and over the entire elevation range as well as a quasi-stochastic component of ~1% about this value. To account for this systematic underestimation of the "true" SIWVs by the reconstruction grid, rooting in the accuracy limit of the pixel-wise summation representing the actual integral, the SIWVs have been "grid matched" by a multiplication factor 0.96 before using them in the reconstruction scheme. In practice, this discretization bias has to be separately estimated for each specific reconstruction grid choice. The quasi-stochastic part was modeled as uncorrelated error of 1% size in SIWV.

Given these three error components, the measurement error covariance matrix S_ε can be written as a sum of three matrices, $S_\varepsilon = S_{\text{dis}} + S_{\text{obs}} + S_{\text{Tm}}$. The diagonal matrix S_{obs} accounts for the uncorrelated component of the observational error, the ith diagonal element is $(0.4 \text{ kg/m}^2 \cdot m(\varepsilon_i))^2$. The matrix S_{Tm} accounts for the T_m-related errors, its ith diagonal element is $(0.01 \cdot \text{SIWV}_i)^2$. However, because of the strong correlations involved, there also exist considerable off-diagonal elements. For approximately modeling these, we exploit the fact that the mean temperature T_m can be interpreted as the atmospheric temperature at a height of ~2 km [*Ross and Rosenfeld*, 1997]. We base the covariance structure model on the locations, where the rays cross the 2 km height level and write

$$S_{\text{Tm } ij} = \sigma_{\text{Tm} i}\sigma_{\text{Tm} j} \cdot \exp\left[-\frac{(x_j^{2\text{km}} - x_i^{2\text{km}})^2}{L_{\text{Tm}}^2}\right], \quad (19)$$

where $x_i^{2\text{km}}$ and $x_j^{2\text{km}}$ are the horizontal ray coordinates corresponding to a height of 2 km, and $\sigma_{\text{Tm} i(\text{or } j)} = 0.01 \cdot \text{SIWV}_{i(\text{or } j)}$. The error correlation length L_{Tm} was adopted as high as 1.5° (~170 km), in order to reflect that significant T_m correlations typically extend over a whole series of stations (given a station spacing of a few 10 km as considered here). The results are found largely insensitive to the specific value of L_{Tm} used, since other (uncorrelated) error components dominate the total measurement error. Finally, S_{dis} is a again a diagonal matrix, capturing the stochastic component of the discretization error. Its ith diagonal element is set to $(0.01 \cdot \text{SIWV}_i)^2$.

6. Imaging Results for Synthetic Data

For basically investigating the performance of the developed imaging algorithm, we directly used SIWV from integration along the different ray paths as input for the retrieval algorithm (compare section 2.2). These simulated SIWV measurements have been randomly disturbed with an RMS of 0.4 kg/m^2 $m(\varepsilon)$, consistent with the uncorrelated observational error described above. In addition, we added a positive bias of $0.01 \cdot$ SIWV to all rays, in order to mimic the T_m-related errors in real SIWVs obtained via the scheme shown in Figure 2 (section 2.6).

As a priori profile we used the mean water vapor density profile over the imaging domain and perturbed it by assuming typical errors for an occultation profile (consistent with the specification of S_{ap}, section 5.1): 10% at the surface increasing to 40% at 10 km, with a vertical error correlation length of 3 km and correlation functions following an exponential decay structure [*Kursinski et al.*, 1995; *Healy and Eyre*, 2000]. Perturbation profiles added to the mean profile
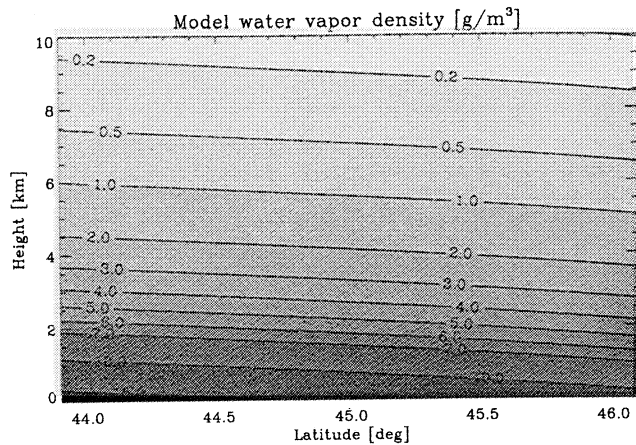
Figure 4. Model water vapor density field ("true") for an exponential atmosphere with linear horizontal gradient.

were generated following the "error pattern superposition" method [*Rodgers*, 2000; section 3.2], which randomly generates profiles statistically consistent with a prescribed error covariance matrix (in the present case, the one associated with the imaging domain center). A representative perturbation profile was selected for the cases shown below, deviating from the mean by up to about one standard deviation. The a priori water vapor density field x_{ap} was then constructed simply by extending the disturbed profile over the entire imaging domain. The latitude range used for the following Figures presenting results was arbitrarily chosen centered at 45°. The covariance matrices S_{ap} and S_ε have been used in the reconstruction scheme (equation (16)) exactly as specified in section 5.

6.1. Exponential Atmosphere With Horizontal Gradient

In this simple but not unrealistic baseline scenario we assumed an exponential decrease of water vapor partial pressure with height and a linear decrease of surface water vapor with increasing latitude, as illustrated by Figure 4. We selected a typical climatological (constant) water vapor scale height of 2 km. The linear latitudinal gradient was chosen in a way that the surface water vapor partial pressure decreased
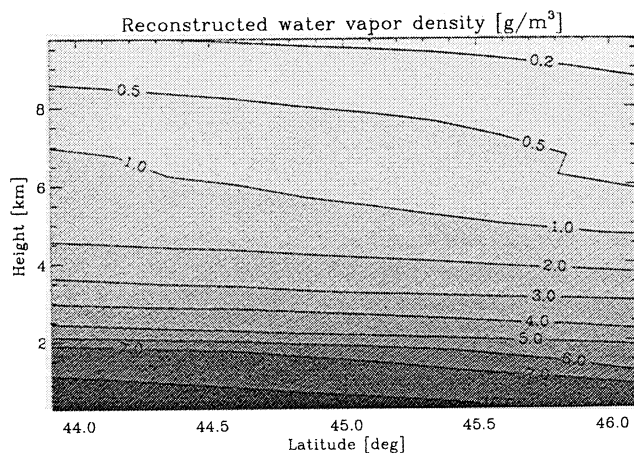

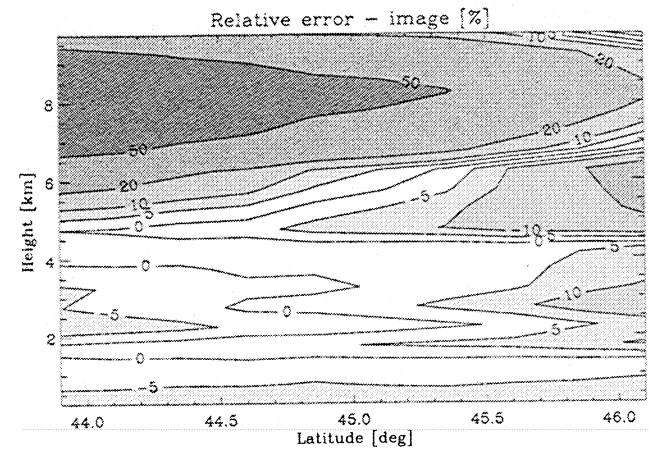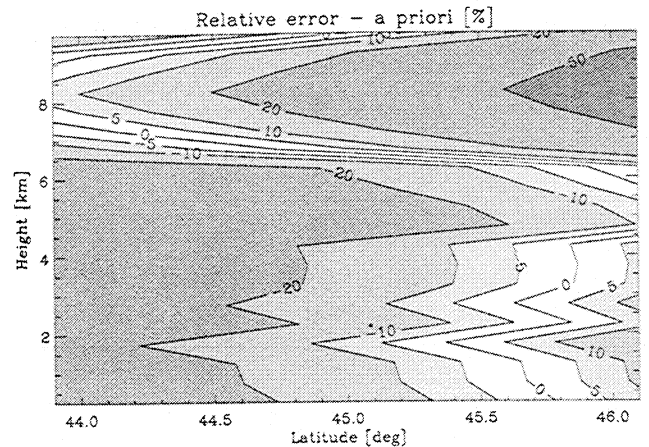**Figure 5.** Optimal estimation image of the model water vapor density field shown in Figure 4.

Figure 6. Relative difference between the a priori field and the "true" field shown in Figure 4 (top) and between the optimal estimation image and the "true" field shown in Figure 4 (bottom), respectively, for the scenario of an exponential atmosphere with linear horizontal gradient.

within the retrieval domain from 25 hPa to 15 hPa (corresponding to water vapor densities from 17.9 g/m³ to 10.9 g/m³, assuming a surface temperature of 20°C).

The optimal estimation reconstruction result is shown in Figure 5. The relative error of the a priori field and of the optimal estimation image are shown in Figure 6. The reconstruction process could not improve upon the prior information above about 6 km in the upper troposphere, where absolute densities are low and thus information contribution from the SIWV measurements is limited. However, below 6 km in the moist lower and mid troposphere, where most information can be gained from the SIWV measurements, the improvement is very significant and both the vertical exponential decay and the horizontal gradient are reasonably well reconstructed.

6.2. Isolated Gaussian Blob

In this scenario we assumed an analytical model water vapor density in the form of a bivariate normal distribution (a so-called "Gaussian blob") with a peak water vapor density of 10 g/m³ at a height of 3 km, a vertical half width of 1 km, and a horizontal half width of 0.15°, respectively. The blob is placed off the center into the right half of the imaging domain. This case serves to indicate the ability and limitations
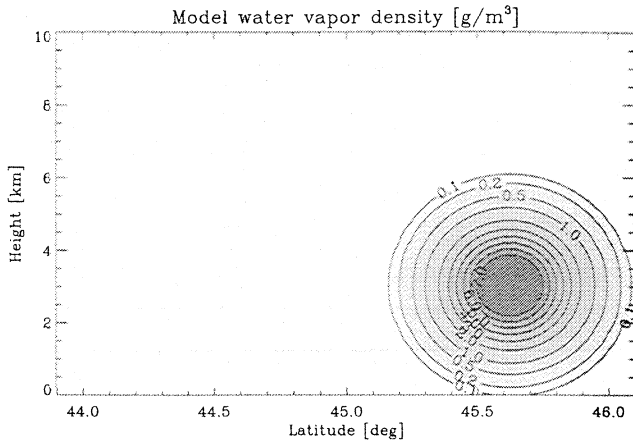
Figure 7. Model water vapor density field ("true" field) for an isolated Gaussian blob.

of the reconstruction algorithm and the adopted pixel sampling to resolve small-scale structures in the water vapor field.

The model water vapor density field ("true" field) is displayed in Figure 7, the corresponding reconstruction result in Figure 8. The overall structure of the Gaussian blob is fairly well resolved, though slightly broadened in latitude. The small-amplitude structures sideward of the Gaussian blob are introduced by the a priori field (the disturbed average profile over the horizontal domain), which is in this case a "Gaussian-layer" structure with a peak water vapor density of 1.1 g/m^2. If the T_m bias, which was assumed positive for the case shown, is assumed negative, the residuals visible in Figure 8 would be slightly reduced.

The errors of the a priori field and of the reconstructed field are shown by Figure 9. In this case, absolute values are displayed, since the quasi-zero density values more than a few half widths away from the peak of the Gaussian blob inhibit the display of relative errors. Figure 9 indicates that again the optimal estimation scheme significantly improves upon prior information and that it allows reasonably well to recover small-scale structures. A series of further synthetic cases have been inspected by *Foelsche* [1999], confirming the robustness
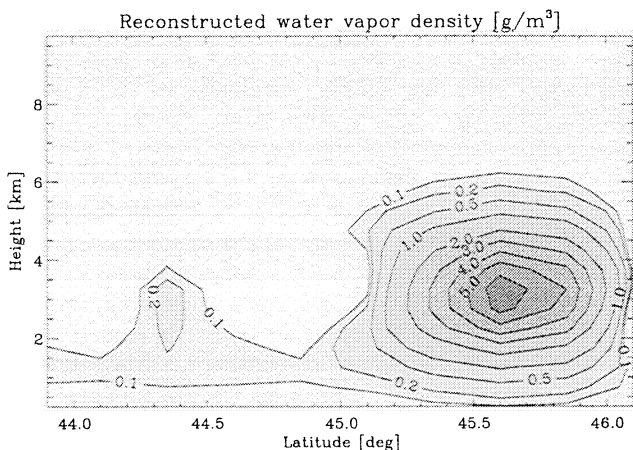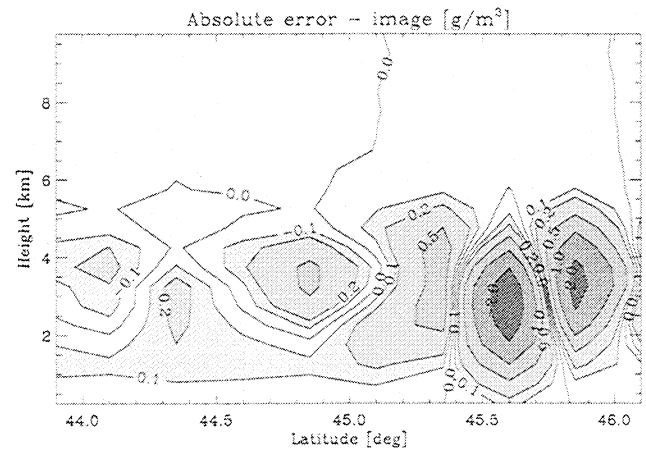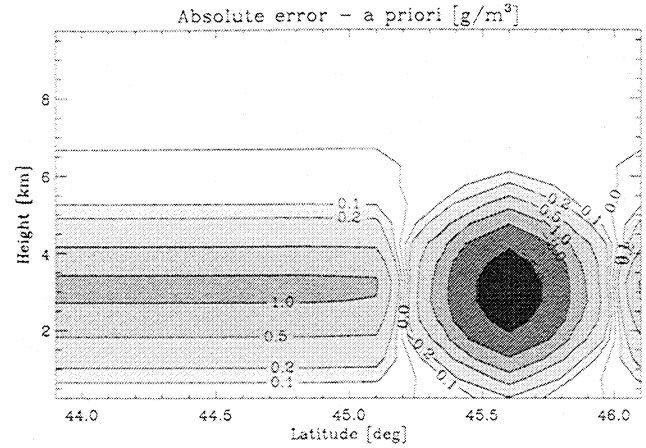

Figure 9. Absolute difference between the a priori field and the "true" field shown in Figure 7 (top) and between the optimal estimation image and the "true" field shown in Figure 7 (bottom) for the scenario of an isolated Gaussian blob.

of the reconstruction scheme but also indicating its resolution limits reached when the scale of a structure starts to be smaller than the spacing between adjacent pixel centers.

7. Imaging Results for ECMWF-Derived Data

7.1. A priori Water Vapor Field

We assumed that a radio occultation measurement colocated with the ground stations delivers an accurate mean refractivity profile, which is representative for the whole imaging domain, as the horizontal range of the domain is comparable to the horizontal resolution of the radio occultation technique. Thus we mimicked occultation-derived refractivity profiles by computing the horizontally averaged profile over the domain. The refractivity profile was perturbed consistent with typical errors for an occultation profile: 1% at the surface linearly decreasing to 0.2% at 10 km [*Kursinski et al.*, 1997], and the correlation function following an exponential decay structure with a vertical error correlation length of 3 km [*Healy and Eyre*, 2000]. Again, the "error pattern superposition" method [*Rodgers*, 2000] was employed to obtain a priori profiles consistent with the a priori error covariance matrix S_{ap}.

Pressure and temperature data from the latest available ECMWF analysis field (3 hours before the field under study)
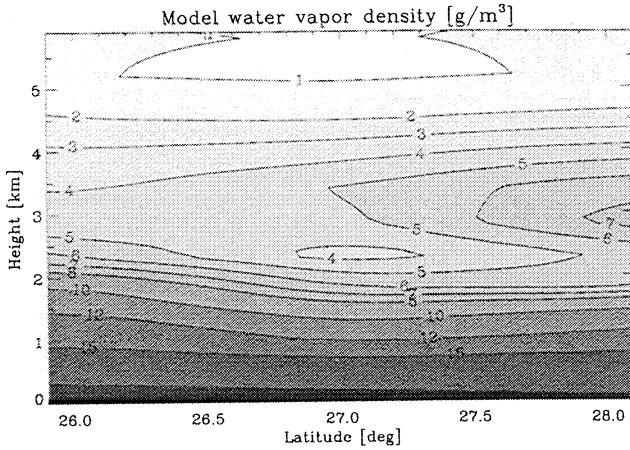

Figure 8. Optimal estimation image of the model water vapor density field shown in Figure 7.

Model water vapor density [g/m^3]

Figure 10. Model water vapor density field ("true" field) for ECMWF T213 analysis data over Florida.

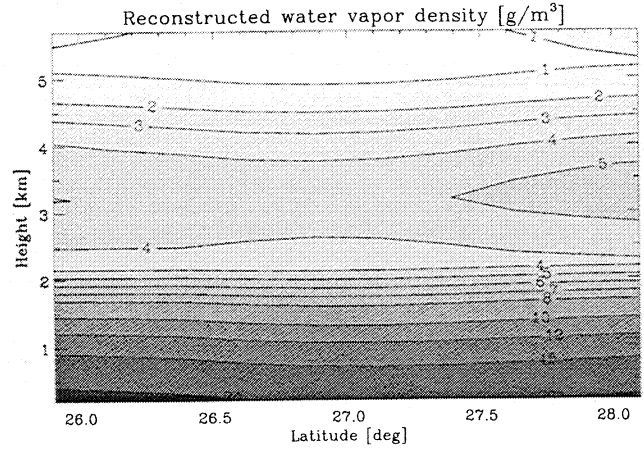Reconstructed water vapor density [g/m^3]

Figure 11. Optimal estimation image of the model water vapor density field shown in Figure 10.

were used to compute a mean dry refractivity profile via the first term on the right-hand side of Equation (1). The water a priori vapor density profile was then obtained via

$$\rho_w(z) = \frac{N_w(z)\, m_w}{\left(k_2 - k_1 + \frac{k_3}{T(z)}\right)R^*} , \qquad (20)$$

where the "wet refractivity" N_w is the part of the refractivity which is attributable to water vapor ($N_w(z) = N(z) - N_d(z)$). We note that using the latest ECMWF analysis to derive pressure and temperature profile information represents a fairly conservative approach; in practice, one would use a short-range forecast.

The obtained a priori water vapor density profile was then assumed to be representative for the entire reconstruction domain (assuming it to be distributed spherically symmetric), furnishing the a priori water vapor density field. An inherent advantage of the radio occultation technique is to deliver a mean profile, which is representative over the entire retrieval domain. In principle, however, any vertical water vapor density profile (e.g., a colocated radiosonde profile) can be used as a good basis for an a priori field as well. The covariance matrices S_{ap} and S_ε were adapted as specified in section 5, with S_{ap} reduced to the domain below 6 km, since only the 12×10 pixels below 6 km are used here (compare section 4).

7.2. Integrated Water Vapor Adjustment

Before applying the reconstruction scheme, equation (16), a useful prerequisite processing step based on the average vertically integrated water vapor (VIWV) data was performed. As the VIWV overlaying a specific station is accurately delivered by the ground-based GNSS measurements, the ten station average VIWV value (after being "grid matched" by the factor 0.96; see section 5.2) was used to adjust (shrink or blow up) the a priori water vapor density profile (equation (20)) in order to match the average VIWV value. We found that by this procedure, which we term "VIWV adjustment" hereinafter, some potential bias in the density profile is effectively mitigated.

As occultation measurements cannot typically be expected to provide data within the first few hundred meters above the surface, a procedure like VIWV adjustment will have to be frequently employed together with short-range vertical extrapolation in order to extend the water vapor density profile reasonably down to the ground. Alternatively, no adjustment at all can be used in this case since it is not a necessary condition in the optimal estimation methodology applied that the a priori field extends over all pixels of the reconstruction domain.

Practically, VIWV adjustment corresponds to multiplying all elements of the a priori field with the same factor f_{adj} (0.8 < f_{adj} < 1.2 typically), matching the vertically integrated columns of the field to the VIWV value. As this adjustment at the same time reduces the uncertainty of the a priori field, also the a priori error covariance elements in S_{ap} need be reduced. Assuming that the uncertainty decreases approximately linearly with the adjustment increment $|1 - f_{adj}|$, we multiply S_{ap} by the factor $(1 - |1 - f_{adj}|)^2$. The a priori profile and
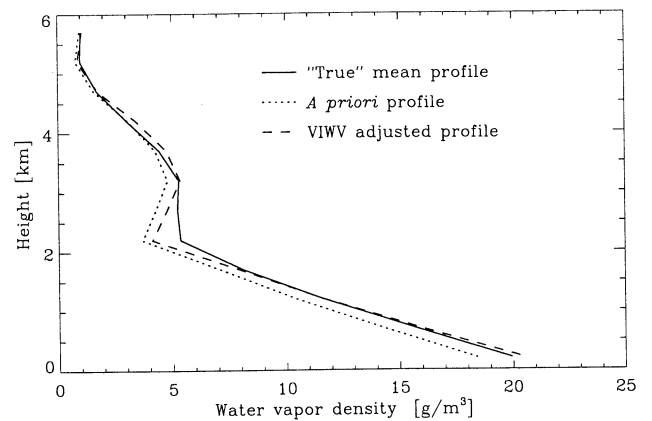

Figure 12. Averaged profile of the model water vapor density field shown in Figure 10 (solid line), density profile obtained by mimicking radio occultation (dotted), and occultation profile after VIWV adjustment (dashed), the latter used as a priori profile (extended over the entire imaging domain).
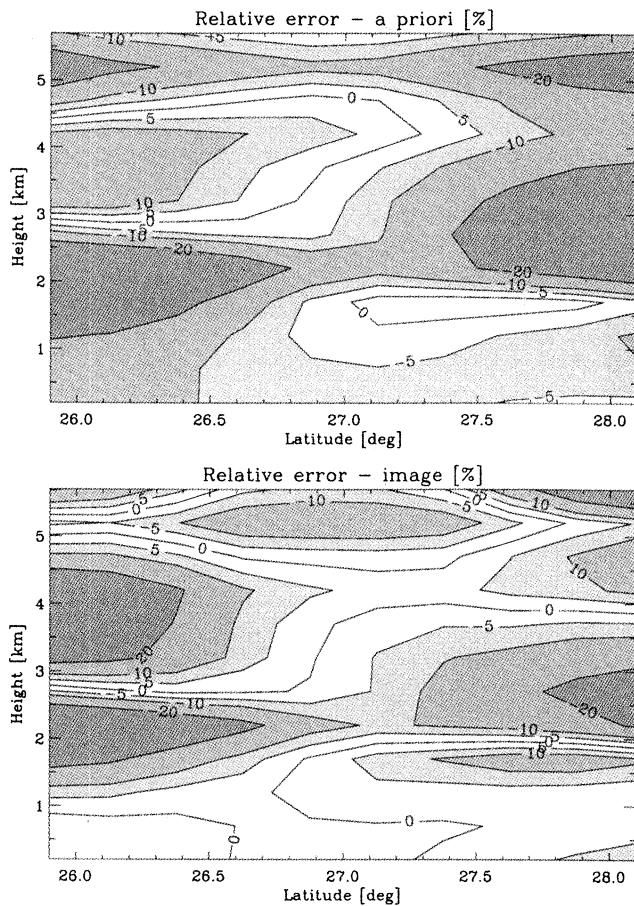
Relative error - a priori [%]

Relative error - image [%]

Figure 13. Relative difference between the a priori field and the "true" field shown in Figure 10 (top) and between the optimal estimation image and the "true" field shown in Figure 10 (bottom),respectively, for the realistic scenario of ECMWF T213 analysis data over Florida.

covariance matrix adjusted this way are then used in the reconstruction scheme, equation (16). While the adjustment of x_{ap} appears to be quite useful, the results are found weakly sensitive to the adjustment of S_{ap}.

7.3. Results for a Low-Latitude Case

Imaging results for an ECMWF-derived refractivity field located over Florida (centered near Palm Beach, at 27°N, 80°W) are presented as a representative example for low-latitude results with a rather moist troposphere. The model water vapor density field is displayed in Figure 10 and the reconstruction result in Figure 11, respectively. A pronounced secondary maximum at a height of ~3 km (toward the northern edge of the reconstruction domain, see Figure 10), associated with the boundary of the trade wind inversion, is clearly visible and reasonably resolved though blurred and therefore underestimated in magnitude in the reconstructed water vapor density field (see Figure 11).

Figure 12 illustrates the behavior of the VIWV adjustment procedure in comparing the "true" profile, the a priori profile (a typical statistically perturbed profile), and the VIWV-adjusted profile, respectively. In this case, where the factor f_{adj} was found to be ~1.15, the adjustment has markedly improved the a priori profile toward the "true" mean profile below about

3 km, which in turn improved the reconstruction result. On the other hand, Figure 12 indicates in the range above 3 km that an integral adjustment does not necessarily improve the prior profile everywhere in the domain and that large deviations (here around ~2.5 km) cannot be cured.

The relative errors of the a priori field and of the reconstructed image are shown in Figure 13, indicating that the reconstruction process significantly improves upon the prior information in most of the imaging domain below about 4 km. In general, even though this "Florida case" shows considerable structure, the retrieval accuracy is better than 10% in most of the domain. Closer inspection shows that in line with the indications from the synthetic cases, the performance is best in the moist lower troposphere and somewhat degraded at the flanks of small-scale structures and above 5 km.

8. Summary and Conclusions

Tomographic imaging becomes feasible when ground-based GNSS measurements are combined with spaceborne GNSS measurements, which requires colocation of ground receivers and occultation events. We developed a technique for tropospheric water vapor imaging, where the ground-based line integral measurements are combined with an occultation profile employing optimal estimation. Instead of occultations, also other profile data could be used (e.g., from radiosondes or short-range model forecasts).

The imaging algorithm was tested by computing different scenarios with the aid of simulated data, involving realistic error specifications both for the ground-based and the spaceborne data. We conclude that the scheme is capable to reasonably reconstruct realistic atmospheric features like secondary water vapor maxima near the top of the trade wind inversion.

In areas with high absolute humidities, where good a priori profiles are frequently available and where small-scale variations of the water vapor density fields are generally less pronounced, the imaging results are generally of good quality. The introduced VIWV adjustment procedure helps suppress bias-like deviations in a priori fields before they are used in the reconstruction scheme.

In areas with low absolute humidities the accuracy of occultation-derived water vapor profiles is degraded and corresponding a priori fields are more vulnerable to be biased. Under these conditions the VIWV adjustment procedure helps most effectively, and even in relatively dry areas, like in Finland, useful two-dimensional information could be obtained with the presented reconstruction approach [Foelsche, 1999].

We are thus confident that the proposed methodology will find fruitful application to real data and thereby contribute to the provision of much needed information on the regional and global water vapor distribution.

References

Bevis, M., S. Businger, T.A. Herring, C. Rocken, R.A. Anthes, and R.H. Ware, GPS meteorology: Remote sensing of atmospheric water vapor using the Global Positioning System, *J. Geophys. Res.*, *97*, 15,787-15,801, 1992.

Bevis, M., S. Businger, S. Chiswell, T.H. Herring, R.A. Anthes, C. Rocken, and R.H. Ware, GPS meteorology: Mapping zenith wet delays onto precipitable water, *J. Appl. Meteorol.*, *33*, 379-386, 1994.

Brunner, F.K., and M. Gu, An improved model for the dual frequency ionospheric correction of GPS observations, *Manuscr. Geod.*, *16*, 205-214, 1991.

Davis, J.L., T.A. Herring, I.I. Shapiro, A.E.E. Rogers, and G. Elgered, Geodesy by radio interferometry: Effects of atmospheric modeling errors on estimation of baseline length, *Radio. Sci.*, *20*, 1 593-1 607, 1985.

Elgered, G., Tropospheric radio path delay from ground-based microwave radiometry, in *Atmospheric Remote Sensing by Microwave Radiometry*, edited by M.A. Janssen, pp. 215-258, John Wiley , 1993.

Elgered, G., J.M Johansson, B.O. Rönnäng, and J.L. Davis, Measuring regional atmospheric water vapor using the Swedish permanent GPS network, *Geophys. Res. Lett.*, *24*, 2663-2666, 1997.

Foelsche, U., Tropospheric water vapor imaging by combination of ground-based and spaceborne GNSS sounding data, *Wissenschaftl. Ber. 10*, 164 pp. Inst. for Geophys., Astrophys., and Meteorology, Univ. of Graz, Austria, 1999.

Foelsche, U., and G. Kirchengast, Space-time resolution conditions for atmospheric imaging involving GNSS occultation: A quantitative study, *Tech. Rep. ESA/ESTEC-3/1997*, 38 pp., Inst. for Geophys., Astrophys., and Meteorology, Univ. of Graz, Austria, 1997.

Healy, S.B., and J.R. Eyre, Retrieving temperature, water vapor and surface pressure information from refractive-index profiles derived by radio occultation: A simulation study, *Q. J. R. Meteorol. Soc.*, *126*, 1661-1683, 2000.

Hedin, A.E., Extension of the MSIS thermosphere model into the middle and lower atmosphere, *J. Geophys. Res.*, *96*, 1159-1172, 1991.

Hofmann-Wellenhof, B., H. Lichtenegger, and J. Collins, *GPS Theory and Practice*, Springer-Verlag, New York, 1994.

Kursinski, E.R., G.A. Hajj, K.R. Hardy, L.J. Romans, and L.T. Schofield, Observing tropospheric water vapor by radio occultation using the Global Positioning System, *Geophys. Res. Lett.*, *22*, 2 365-2 368, 1995.

Kursinski, E.R., G.A. Hajj, J.T. Schofield, R.P. Linfield, and K.R. Hardy, Observing Earth's atmosphere with radio occultation measurements using GPS, *J. Geophys. Res.*, *102*, 23,429-23,465, 1997.

Leitinger, R., H.P. Ladreiter, and G. Kirchengast, Ionosphere tomography with data from satellite reception of Global Navigation Satellite System signals and ground reception of Navy Naviagtion Satellite System signals, *Radio Sci.*, *32*, 1 657-1 669, 1997.

Lide, D.R. (Ed.), *Handbook of Chemistry and Physics*, 74th ed., CRC Press, Boca Raton, Fl., 1993.

Niell, A.E., Global mapping functions for the atmosphere delay at radio wavelengths, *J. Geophys. Res.*, *101*, 3227-3246, 1996.

Rieder M.J., and G. Kirchengast, Error analysis for mesospheric temperature profiling by absorptive occultation sensors, *Ann. Geophys.*, *19*, 71-81, 2001a.

Rieder M.J., and G. Kirchengast, Error analysis and characterization of atmospheric profiles retrieved from GNSS occultation data, *J. Geophys. Res.*, in press, 2001b.

Rocken, C., R. Ware, T. van Hove, F. Solheim, C. Alber, J. Johnson, and M. Bevis, Sensing atmospheric water vapor with the Global Positioning System, *Geophys. Res. Lett.*, *20*, 2631-2634, 1993.

Rodgers, C.D., Retrieval of atmospheric temperature and composition from remote measurements of thermal radiation, *Rev. Geophys.*, *14*, 609-624, 1976.

Rodgers, C.D., *Inverse Methods for Atmospheric Sounding: Theory and Practice*, 256 pp., World Sci. Publ., Singapore, 2000.

Ross, R.J., and S. Rosenfeld, Estimating mean weighted temperature of the atmosphere for Global Positioning System applications, *J. Geophys. Res.*, *102*, 21,719-21,730, 1997.

Thayer, G.D., An improved equation for the radio refractive index of air, *Radio Sci.*, *9*, 803-807, 1974.

Ware, R., C. Alber, C. Rocken, and F. Solheim, Sensing integrated water vapor along GPS ray paths, *Geophys. Res. Lett.*, *24*, 417-420, 1997.

U. Foelsche and G. Kirchengast, Institute for Geophysics, Astrophysics, and Meteorology (IGAM), University of Graz, Universitätsplatz 5, A-8010, Graz, Austria. (ulrich.foelsche@uni-graz.at; gottfried.kirchengast@uni-graz.at)